

<https://doi.org/10.1038/s44310-026-00112-w>

Highly-accurate manipulation of focal length for circular Airy beams

JingYing Zhang^{1,2}, Wei Zhang¹ ✉, Wei Li^{1,2}, HuiJie Ren^{1,2}, ZhaoWu Liu¹ & WenHao Li¹ ✉

The existing excitation models for circular Airy beams suffer from focal length deviation, which reduces the positioning accuracy of the focal point. Using the principle of Fresnel diffraction, this study investigates the influence of phase aperture diffraction on the focal point of circular Airy beams and establishes a precise focal length control model for inversely solving the phase distribution from the beam focus. On this basis, we design a circular Airy beam with a 10 cm focal length and employ a metasurface to experimentally generate such a beam. The angular spectrum simulation and experimental results demonstrate that the actual focal positions are at 10.034 cm and 10.04 cm, corresponding to deviations of 0.34% and 0.4% from the ideal 10 cm focal length, respectively. In contrast, the existing excitation model yields a focal length of 9.5530 cm, a 4.47% deviation from the ideal value. Therefore, the proposed model significantly improves the focusing accuracy of circular Airy beams. This study is expected to facilitate applications of circular Airy beams in ultra-high-precision laser structuring, laser medicine, microscopic imaging and particle manipulation.

As a structured light field, the Airy beam^{1–4} has attracted considerable attention and research in recent years, holding significant application value in areas such as particle manipulation^{5,6}, laser processing⁷, microscopic imaging^{8,9}, optical bullets^{10,11}, and optical communication¹². When arranged with radial symmetry, the Airy beam can be configured into a circular Airy beam with arbitrary focal length^{13,14}, and its non-diffracting and self-healing properties¹⁵ facilitate stable propagation in free space. Moreover, the circular Airy beam exhibits excellent focusing characteristics, maintaining low intensity along the propagation axis before the focus, and the intensity at the focal point increases by several orders of magnitude. This spatially selective intensity distribution enables precise action within the focal region while minimizing interference along the transmission path. As a result, the circular Airy beam is highly applicable to laser ablation technology^{16,17}, allowing minimally invasive thermal ablation of specific tissues such as the liver, the thyroid, and metastatic lymph nodes, while avoiding damage to adjacent critical structures^{18–20}. Owing to the exceptional focusing properties, circular Airy beams also enable high-precision structural fabrication²¹, precise particle manipulation^{22,23}, and high-resolution microscopic imaging^{24–26}.

Researchers have conducted extensive studies on generating circular Airy beams^{27–29}. For instance, Davis et al.²⁷ used a single spatial light modulator to encode a binary phase within an annular region with an inner diameter of 2.5 mm and an outer diameter of 6.9 mm, generating a circular Airy beam with a focal length of 65 cm. Zhang et al.²⁸ employed an all-dielectric metasurface with an inner diameter of 15 μm and an outer

diameter of 65 μm to achieve an achromatic circular Airy beam in the 450–600 nm wavelength range, with a focal length of 1.3 mm. However, in existing studies on exciting circular Airy beams based on catastrophe theory^{30,31}, the beam focus is primarily defined as the geometric intersection of the parabolic trajectory and the propagation axis. Because of the diffraction effects, the actual focal length deviates from the theoretical design value, leading to a significant reduction in the spatial positioning accuracy of the maximum intensity point. This deviation of the focus adversely affects the precise control of the laser beam in the applications. In laser ablation, even minor focal deviations can compromise surgical precision, leading to unintended damage to healthy tissue. In laser micromachining, focal shift introduces depth errors during drilling and reduces overall machining accuracy³². Moreover, in imaging and particle manipulation, a displaced focus degrades spatial resolution and trapping stability²², directly impacting system performance. Therefore, achieving precise focal control—reducing deviations of the focus—is essential for ensuring process reliability and outcome quality across these high-precision fields. In 2018, Goutsoulas et al.³³ considered the effect of diffraction propagation on the beam focal length and used the Fresnel diffraction theory to analyze the forward propagation, systematically investigating key parameters affecting the focal characteristics. However, this study did not take into account the diffraction effects related to the size of the phase aperture. When the characteristic dimensions of the phase modulator change, the actual focal length may still deviate from the theoretical expectation, and this issue has not yet been effectively resolved.

¹Changchun Institute of Optics, Fine Mechanics and Physics, Chinese Academy of Sciences, Changchun, Jilin, China. ²University of Chinese Academy of Sciences, Beijing, China. ✉e-mail: zhangwei1990@ciomp.ac.cn; liwh@ciomp.ac.cn

Based on the diffraction theory, this study establishes a precise focal length control model for inversely solving the phase distribution of a circular Airy beam from the beam focus. Through the mathematical relationships between the phase aperture and focal length, we obtain a constraint equation for the phase aperture parameters, systematically revealing the influence of phase distribution on the focus and enabling precise control over the focusing of a circular Airy beam. Via multi-parameter co-optimization, we design a circular Airy beam with a 10 cm focal length and fabricate a metasurface to generate it. Experimental results show that the actual focal length is 10.04 cm, deviating from the design target by only 0.4%. This study enables precise control of the focal length of circular Airy beams by establishing a focusing model based on aperture diffraction, promoting their applications in high-precision laser structuring, laser medicine, and particle manipulation.

Results

Precise focal length control model of a circular Airy beam

As depicted in Fig. 1, after phase modulation, the incident plane wave converges along a parabolic trajectory described by the equation³³:

$$r = f(z) = r_0 - a^2 z^2, \tag{1}$$

where r is the radial coordinate in the propagation space, r_0 is the inner diameter of the phase plate, and a is related to the trajectory curvature. From the perspective of geometric optics, the geometric intersection $z_c = \sqrt{r_0}/a$ of the parabolic trajectory and the propagation axis can be obtained by setting $r = 0$, which is treated as the focal point.

To construct a circular Airy beam with a parabolic trajectory, the light rays must be emitted along the trajectory tangent. The optical path δ provided by the phase plane is perpendicular to the light ray direction. This can be described as $d\delta/d\phi$ equal to $df[z(\rho)]/dz$, as shown in Fig.1b. Thus, the phase satisfies³³:

$$\frac{d\phi}{d\rho} = k \frac{d\delta}{d\rho} = k \frac{df[z(\rho)]}{dz}, \tag{2}$$

where ρ represents the radial coordinate of the phase plane, k denotes the wave vector, and ϕ represents the phase distribution.

Integrating the above equation yields the expression for the phase distribution:

$$\phi(\rho) = -\frac{4}{3}ka(\rho - \rho_0)^{3/2}, \tag{3}$$

where ρ_0 is equal to the inner diameter of the phase plate.

Based on the theory of geometric optics, the intersection of the beam trajectory with the propagation axis is considered the focal point of the circular Airy beam. However, the actual focal position is influenced by diffraction during propagation. Therefore, the Fresnel diffraction formula is employed to describe the propagation dynamics of the beam:

$$\psi(r, \theta) = \frac{ke^{i(kr^2/2z)}}{iz} \int_0^\infty \rho \psi_0(\rho) J_0\left(\frac{kr\rho}{z}\right) e^{i(k\rho^2/2z)} d\rho, \tag{4}$$

where r represents the radial coordinate in the propagation space, and $\psi_0(\rho) = A(\rho)e^{i\phi(\rho)}$ represents the complex amplitude distribution at the incident plane.

To derive the expression for the focal position of the circular Airy beam, we set $r = 0$ and perform a third-order Taylor expansion of the total phase $\Psi = \phi(\rho) + k\rho^2/2z$ in the Fresnel integral around $z = z_c + \delta z$. The complex amplitude of the circular Airy beam near the focus is then calculated using the stationary phase approach. The specific expression is³³:

$$\psi(0, \delta z) = A \left(\frac{2\kappa}{k}\right)^{1/3} \frac{2\pi k \rho z}{iz} e^{i\Xi} Ai\left[(2k^2\kappa)^{1/3} g \delta z\right], \tag{5}$$

where, $\Xi = \phi(\rho) + \frac{k\rho^2}{2z_c} - \frac{kg^2(z_c)}{2}\delta z$, $\kappa(z) = \left|\frac{d^2f(z)}{dz^2}\right| = 2a^2$ is the trajectory curvature, and $g = df(z)/dz = -2a^2z_c$ is the trajectory slope. Because the maximum of the Airy function corresponds to -1 , we can substitute this value into Eq. (5) by setting $(2k^2\kappa)^{1/3} g \delta z = -1$ to obtain the accurate focal length expression for circular Airy Beam³³:

$$z_f = z_c + \delta z = z_c - \frac{1}{[2k^2\kappa(z_c)]^{1/3} g(z_c)} \tag{6}$$

As can be seen from Eq. (6), the focal length is modified by a term δz that is inversely proportional to the trajectory curvature and slope, rather than being simply determined by the convergence point of the trajectory:

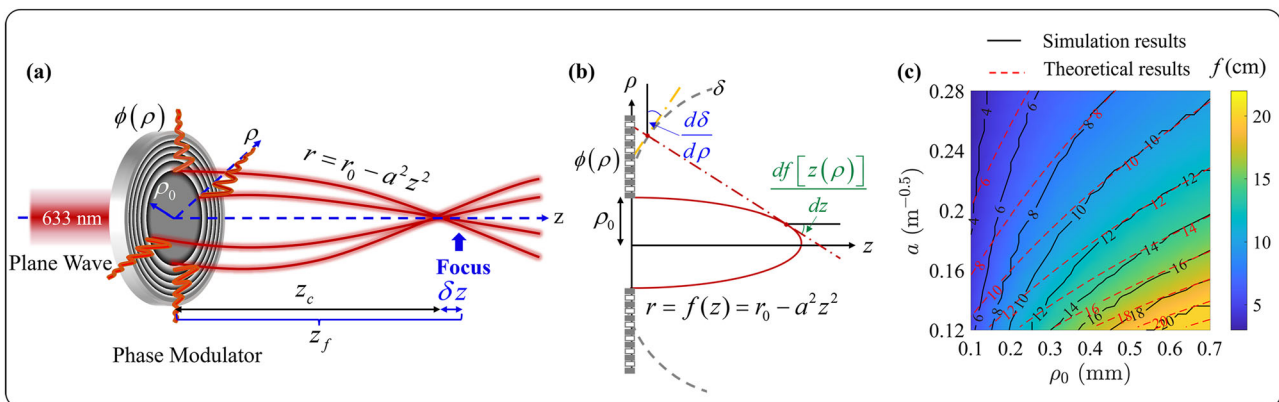


Fig. 1 | Focusing model of a circular Airy beam based on Fresnel diffraction theory. **a** Diagram of the circular Airy beam focusing model, where z_c represents the distance from the convergence point of the parabolic trajectory to the phase plane along the propagation axis, z_f denotes the focal length of the circular Airy beam, and δz indicates the focal length correction term. **b** Diagram of the phase derivation from the focus, where δ denotes the optical path difference, $d\delta/d\rho$ and $df[z(\rho)]/dz$ represent the slope of the optical path difference and the parabolic trajectory,

respectively. **c** Analysis of the effect of internal phase aperture on the focal length f , with the horizontal axis representing the internal phase aperture ρ_0 , the vertical axis representing the trajectory parameter a . In the figure, colors correspond to the focal lengths of circular Airy beams simulated using the angular spectrum method under various trajectory parameters. The black solid lines show the focal-length contour of circular Airy beams simulated via the angular spectrum method; red dashed lines show the contour from Eq. (6).

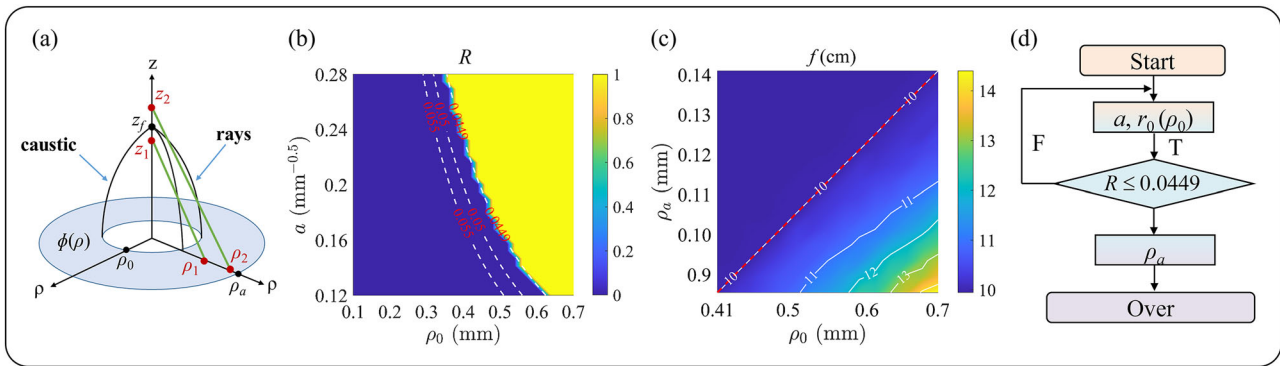


Fig. 2 | Accurate focusing model of a circular Airy beam via phase aperture constraints. **a** Comprehensive schematic of the accurate focusing model with the inner and outer phase apertures. **b** Diffraction effect of the inner radius of the phase

aperture on the focal length. **c** Diffraction effect of the outer radius of the phase aperture on the focal length. **d** Flowchart of the multi-parameter co-optimization process.

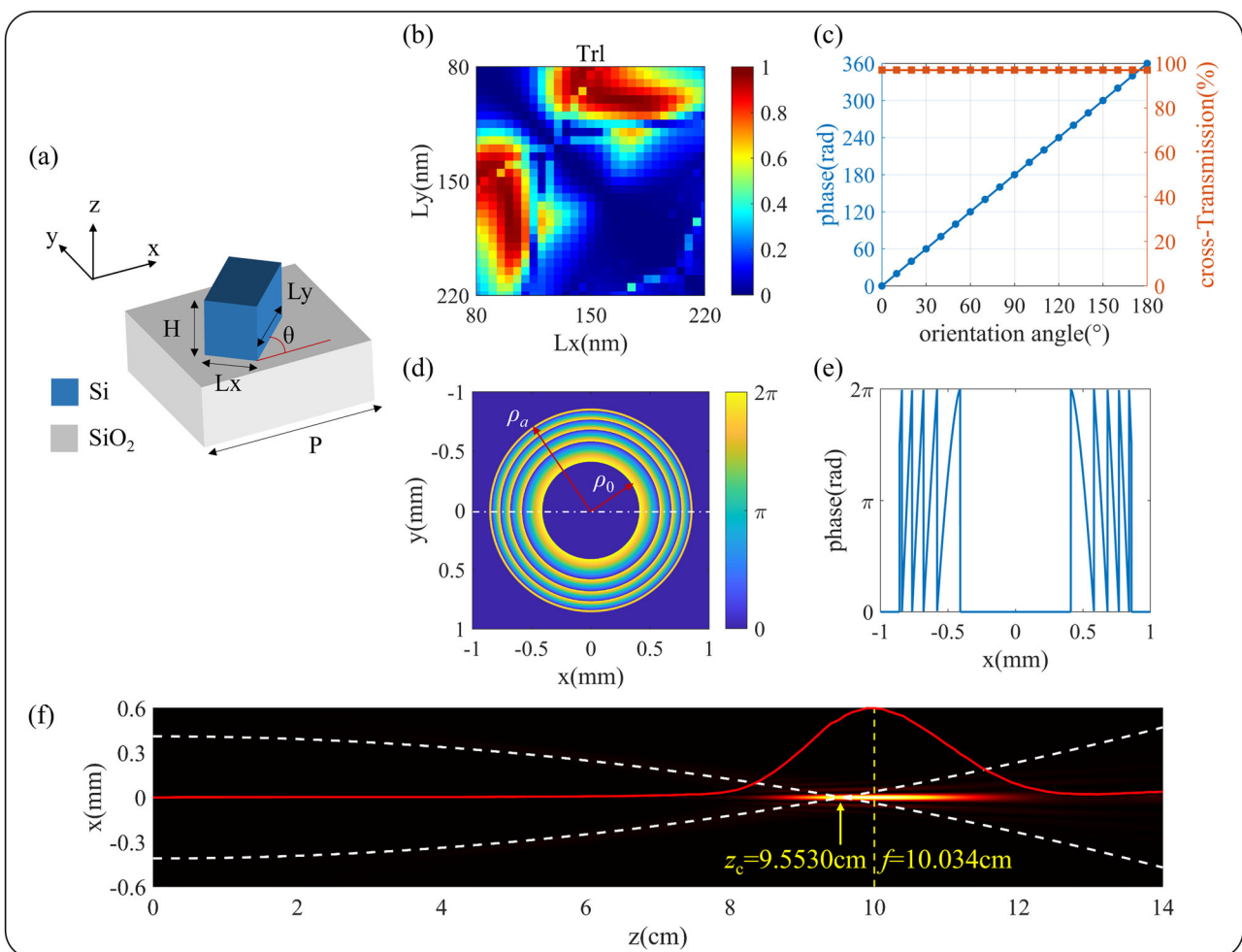


Fig. 3 | Simulate phase distribution and optical field of a circular Airy beam with a 10 cm focal length. **a** Schematic of the metasurface unit cell. **b** Library of polarization conversion efficiency for rectangular unit cells. **c** Plot of geometric phase/efficiency versus rotation angle for the selected unit structure. **d** Phase distribution of

the circular Airy beam with a 10 cm focal length. **e** Plot of the phase cross-section. **f** Side view of the circular Airy beam propagation, showing the focal point at 10.034 cm (the white curved dashed lines indicate the parabolic trajectory of the beam).

$z_c = \sqrt{r_0}/a$. It should be noted that $g(z_c) < 0$, so the focal length of the circular Airy beam is always larger than z_c . Therefore, in theory, parameters can be optimized using Eq. (6) to design a circular Airy beam with precise focal length. However, simulations of the actual focal length using angular spectrum theory with a series of values of the inner radius ρ_0 of the phase plate reveal a systematic deviation from the values calculated using Eq. (6).

Figure 1c shows that for certain values of parameters ρ_0 and a , the theoretical focal length given by Eq. (6) (red dashed lines) deviates consistently from the actual focal length of the beam (black solid lines). In the simulation, the influence of the outer radius of the phase plate on the focal length was eliminated by setting the outer radius to three times the inner radius, to approximate an infinite extent. Thus, to achieve accurate focusing of the

circular Airy beam, it is necessary to develop a comprehensive model that accounts for both the inner and outer radii of the phase plate.

In this work, we used the modified focal length of Eq. (6) to establish an accurate focusing model that comprehensively incorporates the diffraction with the inner and outer phase apertures, as shown in Fig. 2. In deriving the modified focus expression of Eq. (6) from the Fresnel diffraction integral of Eq. (4), the total phase $\Psi = \phi(\rho) + k\rho^2/2z$ in the Fresnel integral is expanded using a third-order Taylor series approximation around $z = z_c + \delta z$. Here, δz represents a small expansion value within the neighborhood of z_c , and is significantly smaller than z_c . Since the inner radius of the phase plate is functionally related to δz . The selection of the inner radius in the Fresnel diffraction-based focusing model is constrained by the allowable range of δz . To quantitatively analyze the effect of δz , we introduce a key parameter ratio $R = \delta z/z_c$ and perform calculations for different inner radii, are shown in Fig. 2b. The yellow area in the figure indicates that the theoretical calculation results are consistent with the simulation results, while the blue area represents that there is a deviation between two terms, and the contour lines depict the calculated R values in different inner radii. Theoretical simulations reveal that when $R \leq 0.0449$, corresponding to $\delta z \leq 0.0449z_c$, the theoretical formula agrees perfectly with the simulation results. This provides a clear mathematical criterion for optimizing the inner radius of the phase plate.

Furthermore, we study the influence of the diffraction from the outer radius of the phase mask on the focal distance of the circular Airy beam. According to catastrophe theory, for a caustic surface to form, the phase Ψ in the Fresnel integral must satisfy $\partial_\rho \Psi = 0$ and $\partial_{\rho\rho} \Psi = 0$. From $\partial_\rho \Psi = 0$, we derive the relationship between the emission position ρ on the phase plane and the propagation position z of the circular Airy beam as: $k\rho/z + \phi'(\rho) = 0$. This equation includes two solutions on the phase surface: ρ_1 and ρ_2 , corresponding to the rays that make the dominant contribution to the propagation position z , where $\rho_1 < \rho_2$, as illustrated in Fig. 2a. From $\partial_{\rho\rho} \Psi = 0$, we derive the expression for the spatial position ρ_j of the light ray emitted from the phase plane as: $z_j = -k/\phi''(\rho_j)$, where $z_1 < z < z_2$. For the focal position z_f , there are two radial positions ρ_1 and ρ_2 on the input plane corresponding to the rays that make the dominant contribution to the focal point, and there exists an inequality constraint $z_1 < z_f < z_2$, it follows from the inequality $z_2 = -k/\phi''(\rho_2) > z_f$, from which we can drive:

$$\rho_2 > (z_f a)^2 + \rho_0. \tag{7}$$

To ensure sufficient ray interference at the input plane for forming a circular Airy beam with focal length z_f , the phase plate must include at least the ray originating from ρ_2 , i.e., $\rho_a > \rho_2$. This leads to the derived constraint on the outer radius of the phase plate:

$$\rho_a > (z_f a)^2 + \rho_0. \tag{8}$$

To validate the theoretical formula (8), we simulate the focal distance of circular Airy beams with varying outer radii of the phase mask, using a designed focal length of 10 cm and selecting trajectory parameters within the specified range $\delta z \leq 0.0449z_c$, as illustrated in Fig. 2c. The red dashed line in the figure indicates the critical minimum outer radius calculated by Eq. (8). As can be observed from the figure, when the outer radius of the phase mask exceeds the critical value, the measured focal length remains strictly consistent with the theoretical design value of 10 cm. However, when the outer radius falls below the critical value (below the red dashed line), the actual focal length obtained from angular spectrum simulations significantly deviates from the designed 10 cm value because of aperture diffraction effects. Thus, we have established definitive criteria for the inner and outer radii phase parameters and developed a co-optimization process of multiple parameters to precisely design a precise focal length circular Airy beam

[Fig. 2d]. The details are as follows:

$$\begin{aligned} \text{objective functions : } & \begin{cases} z_f = z_c + \delta z \\ \phi(\rho) = -\frac{4}{3}ka(\rho - \rho_0)^{3/2} \end{cases} \\ \text{restrictive conditions : } & \begin{cases} R \leq 0.0449 \\ \rho_a > (z_f a)^2 + \rho_0 \end{cases} \end{aligned} \tag{9}$$

Study on the light field of circular Airy beams with a 10 cm focal length

Using the precise focusing model, we design a circular Airy beam with a focal length of 10 cm. Using multi-parameter cooperative optimization, we obtain the trajectory parameters $r_0 = 0.41$ mm and $a = 0.21196$ m^{-0.5}, where the intersection of the trajectory with the propagation axis based on the geometric optics is $z_c = 9.5530$ cm. According to Eq. (8), we select a minimum outer radius $\rho_a = 0.86$ mm for the phase plate. Substituting the above parameters into Eq. (3) yields the phase distribution, as shown in Fig. 3d. And we encode this phase onto a metasurface to experimentally generate a circular Airy beam.

When the unit structure is rotated by an angle θ , the corresponding Jones matrix can be expressed as³⁴:

$$T(\theta) = R(-\theta)T_0R(\theta) = \begin{bmatrix} \cos \theta & -\sin \theta \\ \sin \theta & \cos \theta \end{bmatrix} \begin{bmatrix} t_x & 0 \\ 0 & t_y \end{bmatrix} \begin{bmatrix} \cos \theta & \sin \theta \\ -\sin \theta & \cos \theta \end{bmatrix} \tag{10}$$

where $R(\theta)$ is the rotation matrix, t_x and t_y represent the complex transmission coefficients of the x - and y -linearly polarized light beams passing through the unit cell.

When the circularly polarized light is incident, the transmitted beam can be expressed as^{35,36}:

$$T_c(\theta) = T(\theta) \begin{bmatrix} 1 \\ \pm j \end{bmatrix} = \frac{t_x + t_y}{2} \begin{bmatrix} 1 \\ \pm j \end{bmatrix} + \frac{t_x - t_y}{2} e^{\pm j2\theta} \begin{bmatrix} 1 \\ \mp j \end{bmatrix} \tag{11}$$

where $\psi = 2\theta(x, y)$ represents the geometric phase of the unit cell, and $\left| \frac{t_x - t_y}{2} \right|^2$ represents the polarization conversion efficiency of the unit cell.

For a rectangular silicon unit cell with a period $P = 300$ nm and height $H = 480$ nm located on the SiO₂ substrate (Fig. 3a), we employ the finite-different time-domain (FDTD) method to simulate the polarization conversion efficiency of rectangular unit cells with different dimensions at a wavelength of 633 nm, as shown in Fig. 3b. From the results, we select the unit cell with the highest polarization conversion efficiency. This cell is 170 nm in length and 100 nm in width, and achieves a polarization conversion efficiency of 97%. By rotating the unit cell in 10° steps from 0° to 180°, we simulate the phase response and efficiency of the cross-polarized state, as shown in Fig. 3c. The results demonstrate that the phase response of the selected unit cell varies linearly with the rotation angle, whereas the efficiency remains consistent across the entire range. Then, by changing the rotation angles of the unit cell, we obtain a metasurface with the phase distribution in Fig. 3d.

Using angular spectrum method, we numerically simulate the light fields of the circular Airy beams in free space, as shown in Fig. 3f. The figure shows that the beam energy propagates along the parabolic trajectories, with the intensity peak appearing behind ($z_f = 10.034$ cm) the intersection of the trajectory with the propagation axis ($z_c = 9.5530$ cm), where the minimum interval of z values is 10 μm during the simulation. The relative error between the measured focal length and the design value of 10 cm $|(z_f - z_{ideal})/z_{ideal}|$ is 0.34%. This deviation stems from the higher-order truncation when applying Taylor expansion to the total phase during the calculation using the Fresnel diffraction formula (4). In comparison, the deviation between the focal point z_c from geometric optics and the actual focal point $|(z_c - z_{ideal})/$

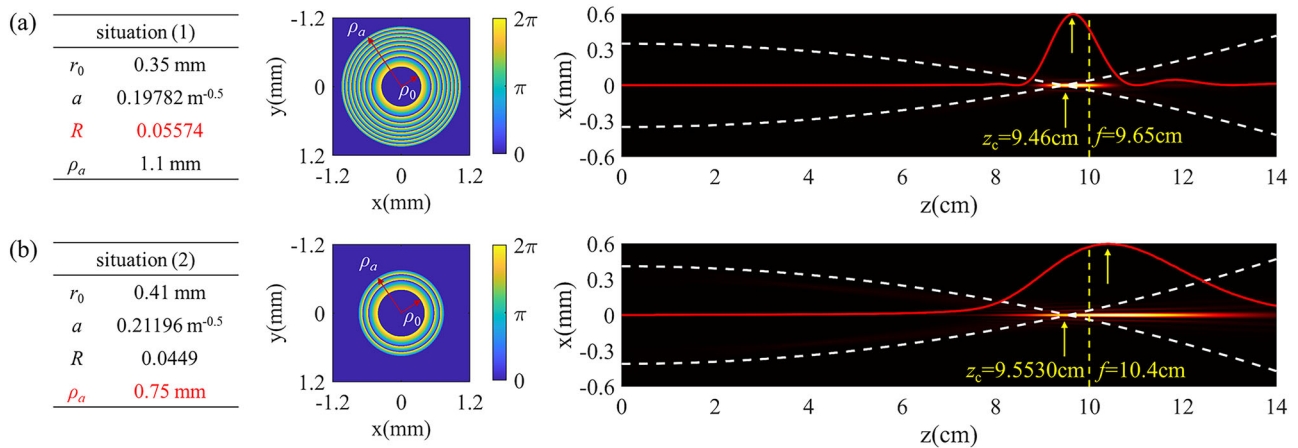


Fig. 4 | Simulation of the x-z axial side-view intensity distributions of circular Airy beams under different phase aperture parameters. a Specific parameters, phase diagram, and the beam propagation process when the inner phase aperture

fails to satisfy the condition $R \leq 0.0449$. **b** Specific parameters, phase diagram, and the beam propagation process when the outer phase aperture does not fulfill the requirement $\rho_a > (z_f a)^2 + \rho_0$.

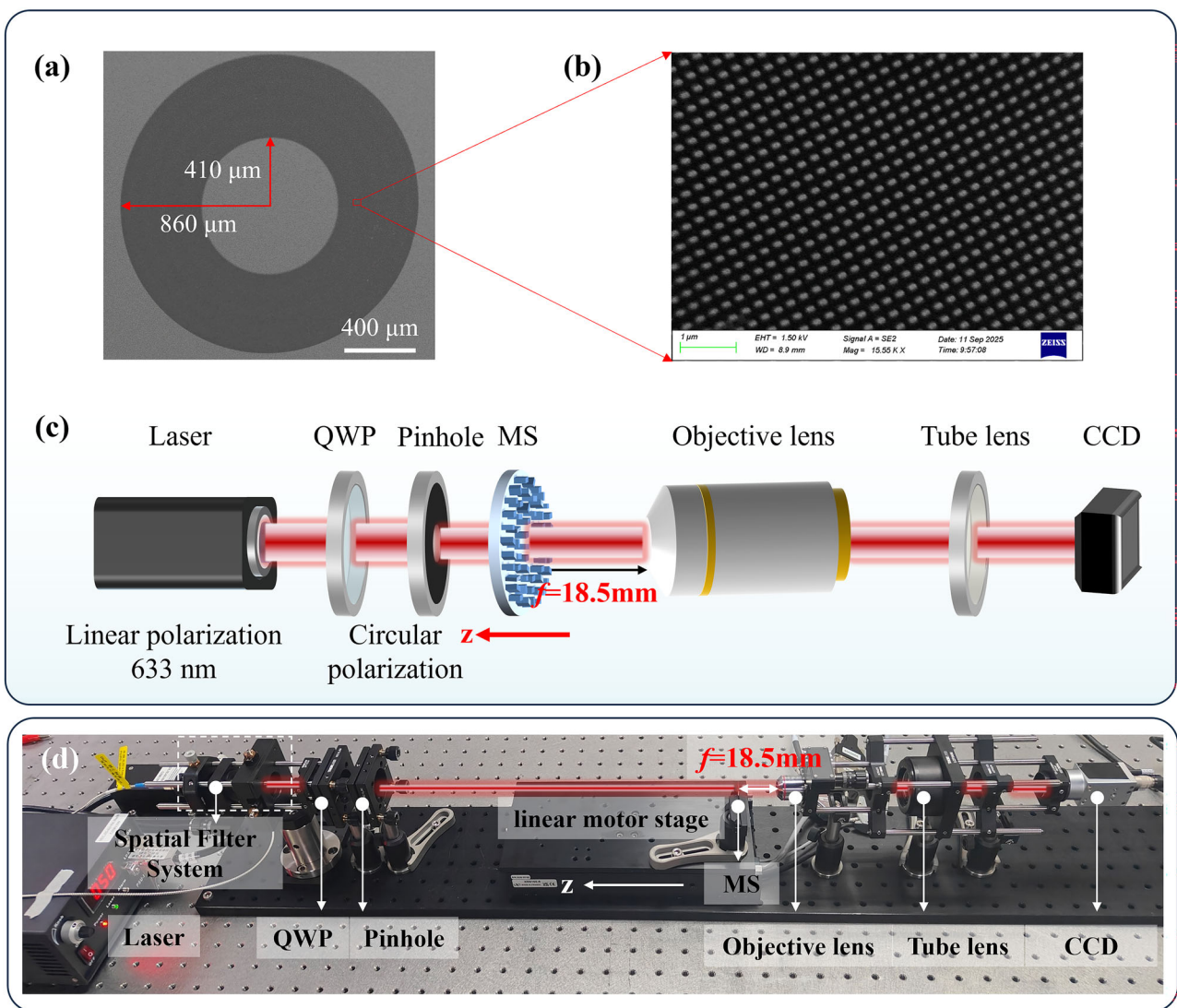


Fig. 5 | SEM images of the metasurface and diagram of the experimental optical path. a SEM image of the metasurface and **b** its magnified view. **c** Diagram of the experimental optical path. QWP: quarter-wave plate. MS: metasurface. The

microscopic measurement system consists of an objective lens, a tube lens, and a CCD camera. The metasurface is installed on a linear motor stage that moves along the z-direction. **d** Picture of the experimental optical path.

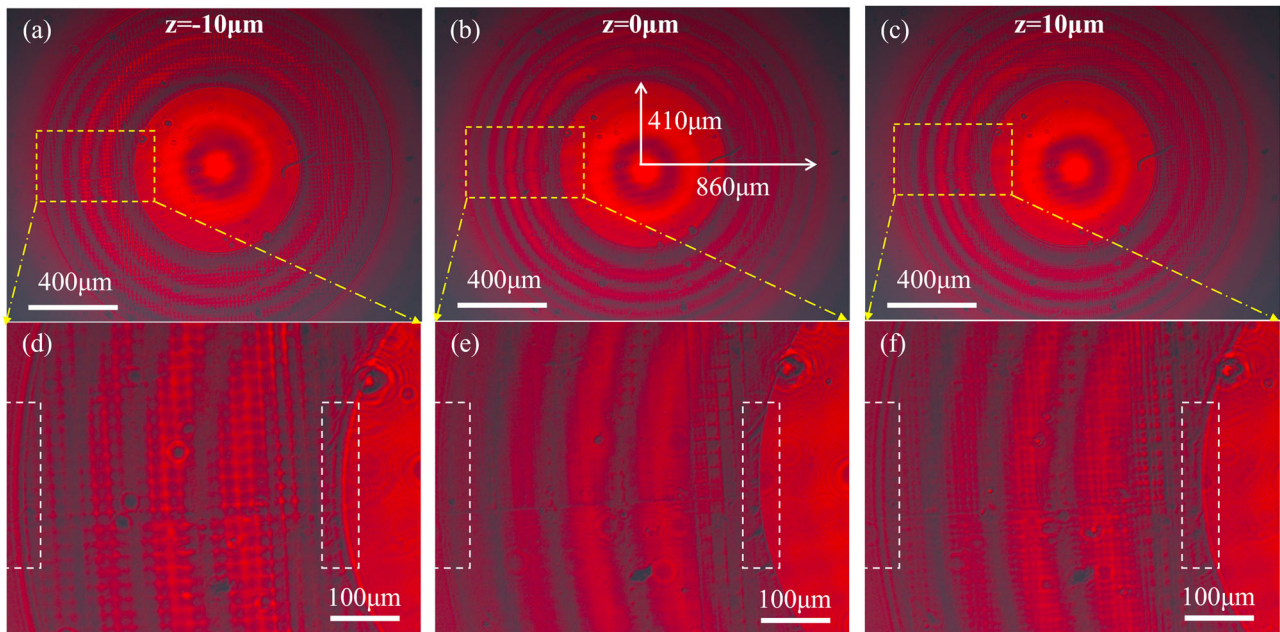


Fig. 6 | Optical field distribution during the zero calibration of the metasurface. **a** Optical field distribution when the metasurface is located 10 μm before the zero position; **b** Optical field distribution when the metasurface is at the zero position;

c Optical field distribution when the metasurface is located 10 μm after the zero position; **d–f** Corresponding magnified views.

z_{ideal} is 4.47%, indicating that this model significantly improves the focusing accuracy of the circular Airy beam.

Furthermore, we consider the two restrictive conditions of the phase plate dimensions for the designed focal length of 10 cm: (1) the phase plate dimensions do not satisfy the condition $R \leq 0.0449$; (2) the phase plate dimensions satisfy $R \leq 0.0449$ but fail to meet the condition $\rho_a > (z_f a)^2 + \rho_0$. Then we calculate the x - z cross-sectional optical field distributions of the circular Airy beams, as shown in Fig. 4. As can be seen from the figure that the beam still follows a parabolic trajectory toward the focus and maintains low intensity along the z -axis before the focus. However, the specific geometry of the parabola varies with different parameters, with parabolic geometry variation of different parameters. Because the phase plate dimensions do not meet the requirements, the actual focal points shift forward to 9.65 cm (situation (1)) and backward to 10.4 cm (situation (2)), corresponding to deviations of 3.5% and 4% from the designed focal length of 10 cm. These results further confirm that the dimensional constraints of the phase plate primarily affect the longitudinal focal position of the beam, rather than its intrinsic propagation characteristics. Therefore, the restrictive conditions and optimization model proposed in this work fundamentally serve to enable precise control over the focal point while ensuring the stability of the beam’s propagation properties.

Experimental results and analysis

Figure 5a, b shows scanning electron microscopy (SEM) images of the metasurface. Figure 5c, d shows a diagram and experiment of the optical path. A 633 nm linearly polarized beam with the spot size of 2 mm emitted from a laser first passes through a spatial filter system to produce clean plane beams with the spot size of 7.2 mm, then manipulated by a quarter-wave plate, a 2 mm pinhole, and impinges perpendicularly onto the metasurface. After passing through the metasurface, the beam is modulated to generate a circular Airy beam. We use a microscopic measurement system consisting of a 4× objective lens ($NA = 0.1, f = 18.5$ mm), a tube lens ($f = 180$ mm), and a CCD camera with a resolution of 4024×3036 and a pixel size of 1.85×1.85 μm (acA4024, Basler) to characterize the optical field distribution of the circular Airy beam. The metasurface is fixed on a linear motor stage (XMS160-S, Newport) with a travel range of 160 mm and a

bidirectional repeatability accuracy of ± 0.04 μm to enable scanning measurements along the z -direction, thereby mapping the axial intensity distribution.

To ensure the accuracy of the measurement, we calibrate the zero position of the metasurface. In the calibration process, the microscopic measurement system (comprising the objective lens, tube lens, and CCD) is first secured. The position of the motor stage is then adjusted in the step of 1 μm, while observing the image captured by the CCD, as shown in Fig. 6. The adjustment continues until the distance between the front surface of the objective lens and the metasurface equals the focal length of the objective lens $f = 18.5$ mm [Fig. 5c, d]. At this point, a clear ring-shaped spot with an inner radius of 410 μm and an outer radius of 860 μm appears on the CCD [Fig. 6b]. When the metasurface deviates from the focal point of the objective lens by 10 μm, diffraction clearly occurs at the edges of the ring-shaped spot within the white dashed boxes in Fig. 6d, f. When the metasurface is positioned at the focal plane of the objective lens, the plane is defined as the $z = 0$ plane. The linear motor stage is then moved to gradually shift the metasurface away from the focal plane of the objective lens, allowing measurement of the beam intensity distribution within the 0–12 cm range.

We employ the linear motor stage with a travel range of 160 mm and a step of 100 μm to conduct 20 repeated measurements of the light field of a circular Airy beam within the range 0–12 cm, as shown in Fig. 7. The on-axis intensity is obtained by extracting the central intensity of the circular Airy beam, as shown in Fig. 7a. The measured result is $f_{Exp} = 10.04 \pm 0.006$ cm (a deviation of 0.4% from the design value). Figure 7b–j shows the results of the 16th measurement. Figure 7b presents on-axis normalized intensity of the circular Airy beam. The experimental results are highly consistent with the simulation results apart from the small noise peaks before the focus, which are caused by the discrete nature of the metasurface unit cells. Figure 7c presents the intensity comparison between z_c and z_f from which we can see that the intensity of z_f is larger than the z_c . Figure 7d presents a comparison between the simulated and experimental one-dimensional normalized intensity profiles at the focal position z_f . The figure shows that the main lobe intensities are highly consistent, while the experimental result exhibits higher sidelobes. Figure 7e–j display the

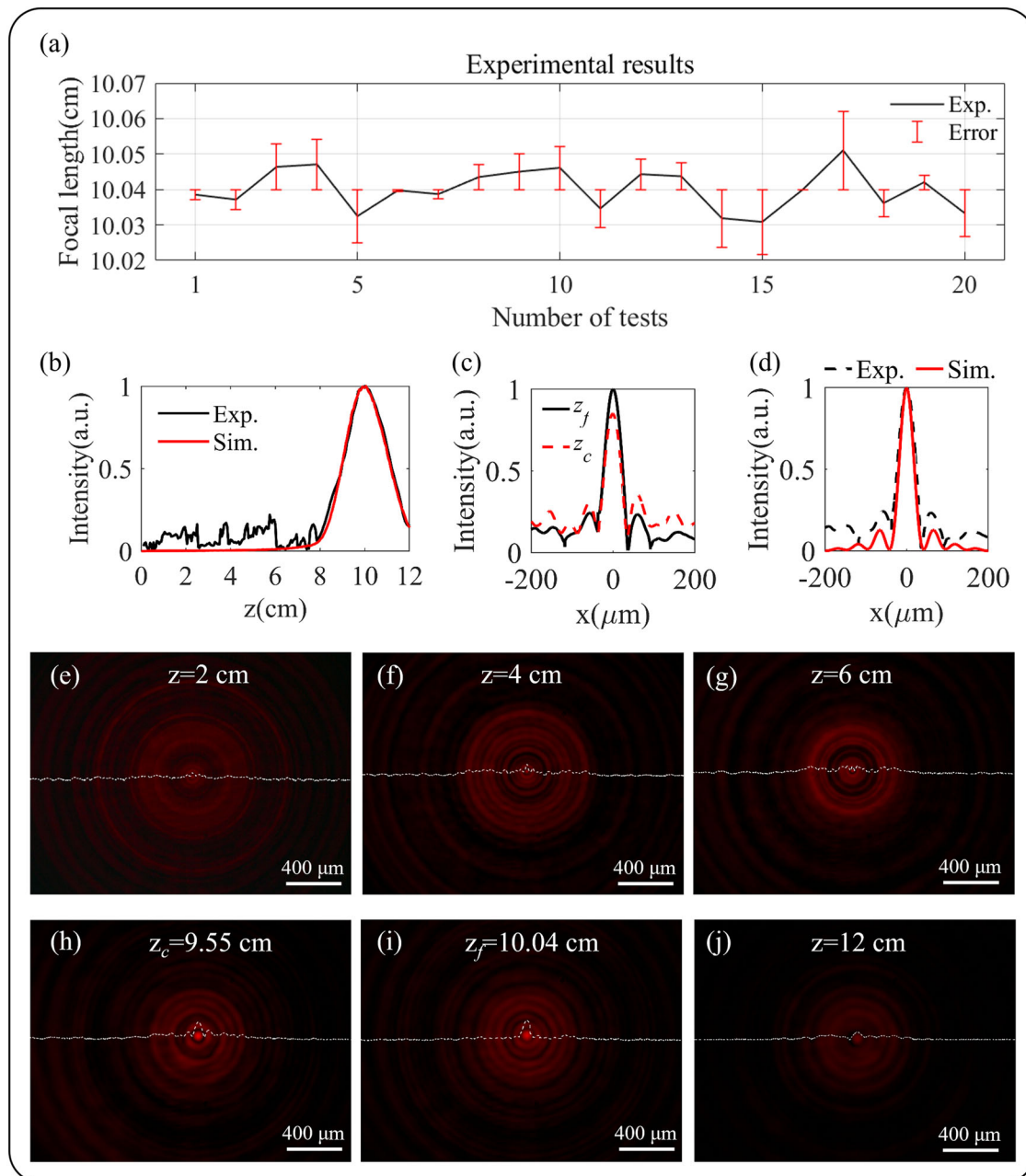


Fig. 7 | Experimental field distribution of the circular Airy beam. **a** Repeated experimental measurements of the focal length. **b** Experimental and simulated axial intensities of the circular Airy beam. **c** Normalized experimental intensity of z_c and z_f . **d** Experimental and simulated one-dimensional intensities along the x -axis at the

focal point of 10.04 cm. **e–j** Experimental two-dimensional intensity distributions of the circular Airy beam at different positions: $z = 2$ cm, 4 cm, 6 cm, 9.553 cm, 10.04 cm, and 12 cm.

experimental two-dimensional intensity distributions at $z = 2$ cm, 4 cm, 6 cm, 9.5530 cm (z_c), 10.04 cm (z_f), and 12 cm, respectively. The results demonstrate that the beam achieves maximum intensity and excellent focusing characteristics at the focal point z_f .

In summary, using the Fresnel diffraction theory, this study constructs a precise focal length control model for inversely solving the phase distribution of circular Airy beams from the beam focus. By systematically investigating the diffraction effects of the phase plate aperture on beam focusing, we define the constraints on the phase aperture, and develop a multi-parameter cooperative optimization model. On this basis, we design and realize a circular Airy beam with a focal length of 10 cm. Both angular spectrum simulations of the beam propagation and experimentation with a metasurface demonstrate a high agreement between the actual

focal position and the designed focal length. The focal length error was reduced from 4.47% to 0.4%. The significance of achieving such a high level of accuracy in focal positioning lies in its direct impact on application performance. In fields such as high-precision laser structuring, laser medicine, and optical particle manipulation, even sub-percent deviations in focal position can lead to noticeable losses in processing resolution, surgical targeting accuracy, or trapping stability. The improvement from 4.47% to 0.4% represents an order-of-magnitude enhancement in positioning accuracy, which effectively enables more reliable and repeatable beam control. This work therefore not only provides a theoretical framework for the precise manipulation of circular Airy beams, but also advances their applicability in scenarios where focal precision is critical.

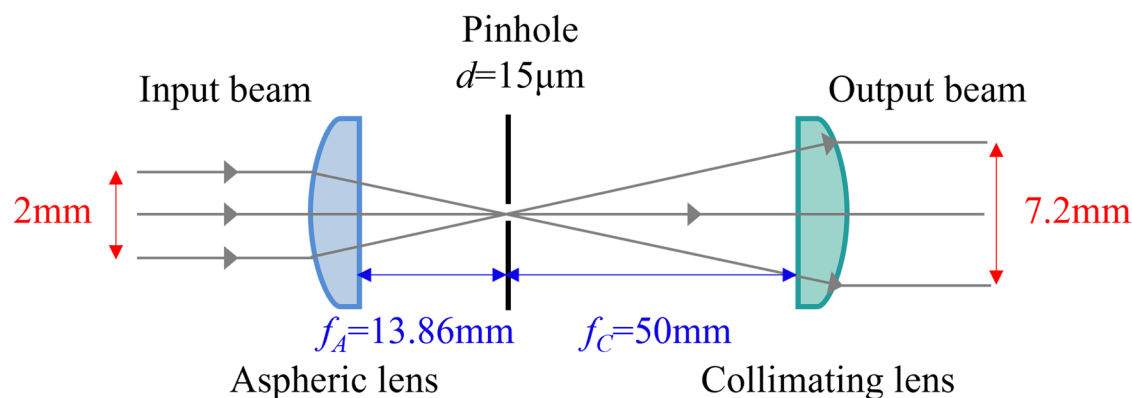


Fig. 8 | Diagram of the spatial filter system.

Methods

Metasurface fabrication

This single-layer metasurface is fabricated through deposition, patterning, lift-off, and etching. First, a 500 µm-thick silicon dioxide substrate is coated with a 480 nm-thick polysilicon film through inductively coupled plasma-enhanced chemical vapor deposition. Following this, a hydrogen silsesquioxane (HSQ, XR-1541) electron beam resist is spin-coated and then baked at 100 °C for 2 min on a hotplate. The desired pattern is defined using a standard electron beam lithography system (Nanobeam Limited, NB5). The development process is carried out in NMD-3 solution (2.38% concentration) for 2 min. Pattern transfer into the polysilicon film is ultimately accomplished via inductively coupled plasma etching (Oxford Instruments, Oxford PlasmaPro 100 Cobra300).

Calculation of beam spot size modulated by a spatial filter system

We use a spatial filter system to expand the input beam and generate the clean plane beam without sidelobes, as shown in Fig. 8. The input Gaussian beam has spatially varying intensity “noise”. When a beam is focused by an aspheric lens, the input beam is transformed into a central Gaussian spot (on the optical axis) and sidelobes, which represent the unwanted “noise”. The pinhole with diameter of 15 µm in the spatial filter system can block the sidelobes and pass the center spot. Then the center spot can be modulated and expanded to a clean plane beam. The diameter of the output beam can be calculated as:

$$D_{out} = \frac{f_C}{f_A} D_{in},$$

where f_C is the focal length of the collimating lens, f_A is the focal length of the aspheric lens, and D_{in} is the diameter of the input beam.

Accuracy limitations of focal length in experimental measurements

During the experimental measurements, the main sources of system error include zero-position calibration error, repeatability accuracy error of the motorized translation stage, and quantization error of CCD. We conducted a quantitative analysis of each error source individually. The maximum error in zero-position calibration was ± 10 µm, while the bidirectional repeatability accuracy of the motorized translation stage was ± 0.04 µm. The quantization error of the CCD is attributed to the limited precision of readout data due to the 8-bit analog-to-digital converter of the CCD. We employed the angular spectrum algorithm to simulate the intensity variation along the z -axis near the focus of the circular Airy beam with a minimum step of 100 µm, 50 µm and 10 µm. The results were normalized relative to 255. With a step size of 100 µm, the CCD can just resolve the variations. Therefore, the quantization error of the CCD is ± 100 µm. In this paper, the CCD quantization error is the primary factor affecting measurement accuracy.

Calculation of focal length in the experiment

Based on repeated measurement results, we define the focal length of the circular Airy beam as:

$$f_{Exp} = \bar{f} \pm s,$$

where the \bar{f} is the mean value of the focal length, f_i is the experimental value of the i -th trial, and s is standard deviation, expressed as:

$$s = \sqrt{\frac{\sum_{i=1}^n (f_i - \bar{f})^2}{n - 1}} (n = 20).$$

Data availability

No datasets were generated or analyzed during the current study.

Received: 3 November 2025; Accepted: 16 February 2026;

Published online: 31 March 2026

References

- Siviloglou, G. A., Broky, J., Dogariu, A. & Christodoulides, D. N. Observation of accelerating Airy beams. *Phys. Rev. Lett.* **99**, 213901 (2007).
- Chen, H., Kludze, A. & Ghasempour, Y. A physics-informed Airy beam learning framework for blockage avoidance in sub-terahertz wireless networks. *Nat. Commun.* **16**, 7387 (2025).
- Voloch-Bloch, N., Lereah, Y., Lilach, Y., Gover, A. & Arie, A. Generation of electron Airy beams. *Nature* **494**, 331–335 (2013).
- Kondakci, H. E. & Abouraddy, A. F. Airy wave packets accelerating in space-time. *Phys. Rev. Lett.* **120**, 163901 (2018).
- Baumgartl, J., Mazilu, M. & Dholakia, K. Optically mediated particle clearing using Airy wave packets. *Nat. Photonics* **2**, 675–678 (2008).
- Cheng, H., Zang, W., Zhou, W. & Tian, J. Analysis of optical trapping and propulsion of Rayleigh particles using Airy beam. *Opt. express* **18**, 20384–20394 (2010).
- Mathis, A. et al. Micromachining along a curve: femtosecond laser micromachining of curved profiles in diamond and silicon using accelerating beams. *Appl. Phys. Lett.* **101**, 071110 (2012).
- Vettenburg, T. et al. Light-sheet microscopy using an Airy beam. *Nat. Methods* **11**, 541–544 (2014).
- Jia, S., Vaughan, J. C. & Zhuang, X. Isotropic three-dimensional super-resolution imaging with a self-bending point spread function. *Nat. Photonics* **8**, 302–306 (2014).
- Chong, A., Renninger, W. H., Christodoulides, D. N. & Wise, F. W. Airy-Bessel wave packets as versatile linear light bullets. *Nat. Photonics* **4**, 103–106 (2010).

11. Zhong, W. P., Belić, M. R. & Huang, T. Three-dimensional finite-energy Airy self-accelerating parabolic-cylinder light bullets. *Phys. Rev. A* **88**, 033824 (2013).
12. Hu, J. et al. A metasurface-based full-color circular auto-focusing Airy beam transmitter for stable high-speed underwater wireless optical communications. *Nat. Commun.* **15**, 2944 (2024).
13. Efremidis, N. K. & Christodoulides, D. N. Abruptly autofocusing waves. *Opt. Lett.* **35**, 4045–4047 (2010).
14. Papazoglou, D. G., Efremidis, N. K., Christodoulides, D. N. & Tzortzakis, S. Observation of abruptly autofocusing waves. *Opt. Lett.* **36**, 1842–1844 (2011).
15. Broky, J., Siviloglou, G. A., Dogariu, A. & Christodoulides, D. N. Self-healing properties of optical Airy beams. *Opt. Express* **16**, 12880–12891 (2008).
16. Døssing, H., Bennedbæk, F. N. & Hegedüs, L. Effect of ultrasound-guided interstitial laser photocoagulation on benign solitary solid cold thyroid nodules—a randomised study. *Eur. J. Endocrinol.* **152**, 341–345 (2005).
17. Pacella, C. M. et al. Thyroid tissue: US-guided percutaneous interstitial laser ablation—a feasibility study. *Radiology* **217**, 673–677 (2000).
18. Mauri, G. et al. Percutaneous laser ablation of metastatic lymph nodes in the neck from papillary thyroid carcinoma: preliminary results. *J. Clin. Endocr. Metab.* **98**, E1203–E1207 (2013).
19. Papini, E. et al. Percutaneous ultrasound-guided laser ablation is effective for treating selected nodal metastases in papillary thyroid cancer. *J. Clin. Endocr. Metab.* **98**, E92–E97 (2013).
20. Mauri, G. et al. Treatment of metastatic lymph nodes in the neck from papillary thyroid carcinoma with percutaneous laser ablation. *Cardiovasc. inter. Rad.* **39**, 1023–1030 (2016).
21. Polynkin, P., Kolesik, M., Moloney, J. V., Siviloglou, G. A. & Christodoulides, D. N. Curved plasma channel generation using ultraintense Airy beams. *Science* **324**, 229–232 (2009).
22. Zhang, P. et al. Trapping and guiding microparticles with morphing autofocusing Airy beams. *Opt. Lett.* **36**, 2883–2885 (2011).
23. Ni, J. et al. Autofocusing capabilities of double-ring circular Airy Gaussian beams and their application in particle manipulation. *Opt. Express* **32**, 44908–44917 (2024).
24. Wang, J., Hua, X., Guo, C., Liu, W. & Jia, S. Airy-beam tomographic microscopy. *Optica* **7**, 790–793 (2020).
25. Chen, L. et al. Optimizing Airy needle-like beams for long-range axial manipulation and super-resolution imaging. *ACS Photonics* **11**, 3610–3620 (2024).
26. Hsu, H. C. et al. Metasurface-based Airy light-sheet fluorescence microscopy. *Appl. Phys. Rev.* **12**, 031412 (2025).
27. Davis, J. A., Cottrell, D. M. & Zinn, J. M. Direct generation of abruptly focusing vortex beams using a $3/2$ radial phase-only pattern. *Appl. Opt.* **52**, 1888–1891 (2013).
28. Zhang, S. et al. Generation of achromatic auto-focusing airy beam for visible light by an all-dielectric metasurface. *J. Appl. Phys.* **131**, 043104 (2022).
29. Cottrell, D. M., Davis, J. A. & Hazard, T. M. Direct generation of accelerating Airy beams using a $3/2$ phase-only pattern. *Opt. Lett.* **34**, 2634–2636 (2009).
30. Berry, M. V. & Upstill, C. IV catastrophe optics: morphologies of caustics and their diffraction patterns. *Prog. Optics* **18**, 257–346 (1980).
31. Kravtsov, Y. A., & Orlov, Y. I. *Caustics, Catastrophes and Wave Fields* (Springer Science & Business Media, 2012).
32. Ho, C. C. et al. Optical emission monitoring for defocusing laser percussion drilling. *Measurement* **80**, 251–258 (2016).
33. Goutsoulas, M. & Efremidis, N. K. Precise amplitude, trajectory, and beam-width control of accelerating and abruptly autofocusing beams. *Phys. Rev. A* **97**, 063831 (2018).
34. Balthasar Mueller, J. P. et al. Metasurface polarization optics: independent phase control of arbitrary orthogonal states of polarization. *Phys. Rev. Lett.* **118**, 113901 (2017).
35. Hong, X. et al. Synthetic nano-kirigami with high deformability for reconfigurable information displays. *Nat. Commun.* **16**, 7843 (2025).
36. Chen, W. T. et al. A broadband achromatic metalens for focusing and imaging in the visible. *Nat. Nanotechnol.* **13**, 220–226 (2018).

Acknowledgements

This study was supported by CAS Project for Young Scientists in Basic Research (No. YSBR-103) and National Natural Science Foundation of China (No. 62525508).

Author contributions

J.Y.Z. performed the theoretical analysis and modeling, experimental tests, analyzed the data, and wrote the manuscript. W.Z. conducted the theoretical analysis, experimental supervision and manuscript review. W.L. and H.J.R. participated in the theoretical discussion. Z.W.L. was engaged in the experimental discussions. W.H.L. proposed ideas, provided experimental support, and conducted manuscript review. All authors read and approved the final manuscript.

Competing interests

The authors declare no competing interests.

Additional information

Correspondence and requests for materials should be addressed to Wei Zhang or WenHao Li.

Reprints and permissions information is available at <http://www.nature.com/reprints>

Publisher's note Springer Nature remains neutral with regard to jurisdictional claims in published maps and institutional affiliations.

Open Access This article is licensed under a Creative Commons Attribution-NonCommercial-NoDerivatives 4.0 International License, which permits any non-commercial use, sharing, distribution and reproduction in any medium or format, as long as you give appropriate credit to the original author(s) and the source, provide a link to the Creative Commons licence, and indicate if you modified the licensed material. You do not have permission under this licence to share adapted material derived from this article or parts of it. The images or other third party material in this article are included in the article's Creative Commons licence, unless indicated otherwise in a credit line to the material. If material is not included in the article's Creative Commons licence and your intended use is not permitted by statutory regulation or exceeds the permitted use, you will need to obtain permission directly from the copyright holder. To view a copy of this licence, visit <http://creativecommons.org/licenses/by-nc-nd/4.0/>.

© The Author(s) 2026